Optical Materials 60 (2016) 513–520

Contents lists available at ScienceDirect

Optical Materials

journal homepage: www.elsevier.com/locate/optmat

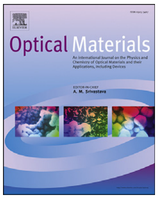

Medical imaging scintillators from glass-ceramics using mixed rare-earth halides

M. Brooke Beckert [a, *], Sabrina Gallego [a], Yong Ding [b], Eric Elder [c], Jason H. Nadler [a]

[a] *Advanced Concepts Laboratory, Georgia Tech Research Institute, USA*
[b] *Institute for Electronics and Nanotechnology, Georgia Institute of Technology, USA*
[c] *Winship Cancer Institute, Emory University, USA*

ARTICLE INFO

Article history:
Received 12 August 2016
Accepted 6 September 2016
Available online 14 September 2016

Keywords:
Glass-ceramic
Nanocomposite
Medical imaging

ABSTRACT

Recent years have seen greater interest in developing new luminescent materials to replace scintillator panels currently used in medical X-ray imaging systems. The primary areas targeted for improvement are cost and image resolution. Cost reduction is somewhat straightforward in that less expensive raw materials and processing methods will yield a less expensive product. The path to improving image resolution is more complex because it depends on several properties of the scintillator material including density, transparency, and composition, among others. The present study focused on improving image resolution using composite materials, known as glass-ceramics that contain nanoscale scintillating crystallites formed within a transparent host glass matrix. The small size of the particles and *in-situ* precipitation from the host glass are key to maintaining transparency of the composite scintillator, which ensures that a majority of the light produced from absorbed X-rays can actually be used to create an image of the patient. Because light output is the dominating property that determines the image resolution achievable with a given scintillator, it was used as the primary metric to evaluate performance of the glass-ceramics relative to current scintillators. Several glass compositions were formulated and then heat treated in a step known as "ceramization" to grow the scintillating nanocrystals, whose light output was measured in response to a 65 kV X-ray source. Performance was found to depend heavily on the thermal history of the glass and glass-ceramic, and so additional studies are required to more precisely determine optimal process temperatures. Of the compositions investigated, an alumino-borosilicate host glass containing 56mol% scintillating rare-earth halides (BaF_2, GdF_3, $GdBr_3$, TbF_3) produced the highest recorded light output at nearly 80% of the value recorded using a commercially-available GOS:Tb panel as a reference.

1. Introduction

1.1. Motivation & purpose

There are a host of medical systems that utilize high-energy X-rays for imaging and therapeutic purposes, including panoramic diagnostic imaging systems used by dentists and linear accelerators that are used to treat cancer patients undergoing radiation therapy. All clinicians that practice with ionizing radiation seek to minimize the dose received by the patient during treatment or diagnostic procedures. However, many scintillating panels currently used to create images from incident X-rays are opaque, and so higher energy X-rays are needed to compensate and maintain image quality. The investigation presented here sought to develop a more transparent scintillator that would facilitate the use of lower energy X-rays without significantly increasing the cost of scintillator panels or compromising image quality.

1.2. Background

Medical X-ray imaging has become a mainstay diagnostic tool for physicians in a variety of fields including dentistry, oncology, mammography, and nuclear medicine. While the fundamental operating principles are similar between fields, each seeks a unique set of diagnostic information and has restrictions regarding the radiation source, dosage, and timing [1]. Thus, image acquisition

---

[*] Corresponding author. 925 Dalney Street, Atlanta, GA 30332, USA.
E-mail address: Brooke.Beckert@gtri.gatech.edu (M.B. Beckert).

http://dx.doi.org/10.1016/j.optmat.2016.09.015
0925-3467/

parameters vary by application, but a majority of diagnostic and therapeutic X-ray imaging systems contain amorphous silicon photodiodes (α-Si) that most efficiently generate images using light in the 400–800 nm range. As a result, most medical imaging scintillators utilize Tb^{3+} as the activator dopant due to their peak emission intensity of 545 nm.

Most imaging panels employ either gadolinium oxysulfide (GOS) phosphors encapsulated in a polymer film [2] or cesium iodide (CsI) single or columnar crystals [3,4] as the light emitter. Both materials require compromise between image quality and cost. For example, GOS panels are inexpensive, but cannot stop high energy X-rays used in therapeutic systems. In contrast, CsI crystals can absorb over 8 MeV X-rays, but are very expensive to fabricate. Thus, significant effort has been devoted to developing alternative scintillator materials that reduce cost with minimal compromise to image quality [5–8]. The present approach opted to use glass-ceramic nanocomposite materials in which nanoscale crystallites of scintillating rare-earth halide are precipitated *in-situ* from an oxide host glass matrix. This allows less expensive, lower purity raw materials to be used, isolates hygroscopic single crystals from environmental moisture, and is conducive to new scintillator geometries and larger imaging panels.

Previous work by the authors [9,10] showed that an alumino-borosilicate (ABS) glass system makes an excellent host for the scintillating halides because it readily forms a transparent, durable glass and has a large network free volume that allows it to accept a high concentration of rare-earth halide scintillating compounds without phase separation. For the scintillating phase, a mixed rare-earth crystal composition, $BaGdF_5$, was chosen to host the Tb^{3+} activators. Recent work in the field has increasingly shown that mixed rare-earth crystals [11,12] can dramatically increase the light output relative to single cation hosts. In this mixed lanthanide crystal, the Ba^{2+} cations act as the sensitizer, while Gd^{3+} cations form an intermediate sublattice along which absorbed energy can migrate until reaching the Tb^{3+} activator [13]. The subsequent energy transfer from Gd^{3+} to Tb^{3+} has been shown to be very efficient for a variety of activators [14].

Although considerable knowledge has been generated to inform the scintillator materials selection process, the behavior and properties of glass-based materials are extremely sensitive to the number and type of constituents used. Therefore, optimization of glass batch composition remains a highly empirical process. Because the primary objective of the present investigation was to maximize scintillator light output, which most directly affects image resolution, three different composition series were designed to determine the compositions that produced the highest light output. First, the total concentration of scintillating rare-earth fluorides was increased until either the solubility limit of the glass was exceeded or light output was degraded. Next, the ceramization schedule for each composition was investigated. Ceramization is a process in which coupons of as-cast glass are re-heated to grow the scintillating crystals in a controlled manner. The dwell period at the ceramization temperature must be optimized to produce an average crystallite size that provides an ordered environment for the activators, but does not cause scattering or absorption of the light emitted. Finally, the ratio of Gd^{3+} to Ba^{2+} was altered to evaluate the dependence of light output on mixed crystal composition.

2. Experimental

2.1. Glass-ceramic synthesis

2.1.1. Glass batching and melting

The glass compositions fabricated for this study are listed in Table 1 (in mol%). The precursor powders were supplied by Alfa Aesar, with Cs_2O and B_2O_3 incorporated as Cs_2CO_3 (99.9%) and H_3BO_3 (99.9%), respectively. The remaining constituents were added as listed in purities of 99.9%.

Each glass formulation was prepared by weighing precise amounts of precursor powders and mixing by hand in a mortar and pestle. After thorough mixing, the powders were loaded into a 250 mL alumina crucible and allowed to dry overnight at 100 °C in air. The dried powder mixture was loaded into a Deltech RS-12 bottom loading glass casting furnace equipped with a 4-inch diameter atmosphere dome. The precursor powders were heated at 4ºC/min to 1450 °C under a light argon purge. The melt was allowed to dwell for two hours at 1450 °C while stirring with an alumina rod, and then cast onto a graphite plate preheated to 500 °C. Cast pieces were annealed overnight at 500 °C to relieve thermal stresses, and then cut into coupons and polished to a mirror finish with diamond abrasives and water prior to characterization and ceramization.

2.1.2. Ceramization of As-cast glass to form glass-ceramic

The ceramization temperature at which scintillating crystallites precipitate was determined via differential scanning calorimetry (DSC). A Netzsch Simultaneous Thermal Analyzer with combination thermogravimetric analysis (TG) and DSC capability was used to determine glass transition and crystallization temperatures for each formulation prepared. Samples of as cast glass were ground into a fine mesh powder and 20 mg packed into a lidded alumina sample crucible. The crucible was loaded into the measurement chamber, and then vacuum pulled before backfilling with a 50 mL/min argon purge. The sample was heated at 5ºC/min to 1400 °C with both TG and DSC data acquired simultaneously. Glass transition regions and crystallization exotherms were identified with Netzsch thermal analysis software. Coupons of polished, as cast glass were heated to the ceramization temperatures identified and held for 2–16 h to determine the time required to achieve peak light output.

2.2. Glass-ceramic characterization

2.2.1. Light output

Perhaps the most important metric for new medical imaging scintillators is the light output produced in response to the X-ray energy used in a given clinical setting. The X-ray energy and exposure time needed to create an image is directly correlated to the dose received by the patient. Physicians seek to reduce this dose to “As Low As Reasonably Achievable” (ALARA) and so a scintillator that can generate an image of equivalent quality using a lower X-ray energy or shorter exposure time will always be preferred. The light output of glass-ceramic scintillators fabricated during this

Table 1
Glass formulations (in mol%) investigated in this study. Total rare-earth (RE-45 through -56) concentration was increased stepwise to determine the solubility limit in the host oxide glass. Then, the ratio of GdF_3 to BaF_2 was first decreased (GD-8) and then increased (BA-30) to evaluate the dependence of mixed crystal composition on light output.

Constituent	RE-45	RE-51	RE-56	GD-8	BA-30
SiO_2	20	19	17	17	17
B_2O_3	15	12	11	12	12
Al_2O_3	12	12	10	10	10
Cs_2O	7	6	6	5	5
BaF_2	24	28	32	33	30
GdF_3	8	9	10	8	10
$GdBr_3$	7	7	7	6	7
TbF_3	6	7	7	9	9

study was measured using a Siemens Heliodent 70 X-ray source with 65 kV, 7 mA beam. The scintillator was installed into a circular sample holder and placed 2.5 mm from the lens of a Watec WAT-902H2 CCD camera. The entire assembly was placed into a light tight box to minimize signal noise due to ambient light. Images were acquired with BlackMagic image acquisition software over a 3.2s exposure time. The frames were exported as an image sequence and then imported into Fiji and stacked with intensity averaged over the stack using Z-projection. The average brightness over the sample was measured and compared to a commercially-available Lanex (GOS:Tb) standard.

2.2.2. X-ray diffraction (XRD)

Phase analysis was performed for glass-ceramic samples exhibiting the highest light output to identify the scintillating phase. An Empyrean X-ray Diffractometer from PANalytical with a Cu-kα source (λ = 0.154 nm) operated at 40 kV and 40 mA was used with a one-half degree anti-scatter slit and 0.04 rad soller slit, with 4 mm filter to reduce the spot size to 10× 10 mm on the sample. The diffraction system is also equipped with a Pixcel detector and a Bragg-Bretano high definition focusing mirror to reduce count time and increase signal. Coupons of cerammed glass were scanned from 10 to 70° (2θ) with a step size of 0.016° (2θ), and resulting patterns were analyzed using HighScore Plus software from PANalytical and compared to standards from the powder diffraction database of the International Centre for Diffraction Data (ICDD).

2.2.3. Transmission electron microscopy (TEM)

Transmission electron micrographs were acquired for select specimens to observe the structure of the as-cast glass and the cerammed glass-ceramic. A Tecnai G2 F30 TEM/STEM operating at 300 kV was used to image each glass and glass-ceramic specimen. Samples were prepared by grinding coupons of as-cast glass and cerammed glass-ceramic into a fine powder with a mortar and pestle. The powder was dispersed in ethanol and deposited onto a carbon coated copper grid using a pipette. Micrographs were acquired in bright and dark field modes.

2.2.4. Photoluminescence emission (PL)

Luminescence measurements were performed to quantify the peak emission and excitation wavelengths of the glass-ceramics. Coupons of polished glass and glass-ceramic (1.5 mm thick) were loaded onto the stage, and then scanned with a Spectra-Physics BeamLok Ar-ion laser and SPEX 1681 0.22m and SPEX 1000M Spectrometers. A 369 nm excitation wavelength was used for PL measurements with a scanning range of 450–650 nm, 1 nm step-size, and one second per step integration time. Excitation measurements were performed using a 545 nm monitor wavelength and scanning between 200 and 400 nm using the same signal integration parameters.

3. Results

3.1. Thermal analysis

The temperature locations of the glass transition region (T_g), scintillating nanocrystal precipitation (T_{ceram}), and devitrification temperature of the host glass matrix (T_{dev}) for each glass formulation were estimated from DSC scans, shown in Fig. 1. Temperatures are presented in degrees Kelvin and DSC signal (in μV) was normalized to allow traces to be superimposed. Batches RE-45, RE-51, and BA-30 did not exhibit distinguishable exothermic crystallization peaks below 1000K in the DSC trace. A pair of convoluted exothermic peaks was observed in the trace for batch GD-8, though a precise crystallite precipitation temperature could not be resolved. A best estimate for ceramization temperature of each composition was determined and listed in Table 2. Each temperature is approximately 150K above the glass transition region. Polished coupons of each formulation were cerammed for 2–16 h at the temperatures listed in Table 2.

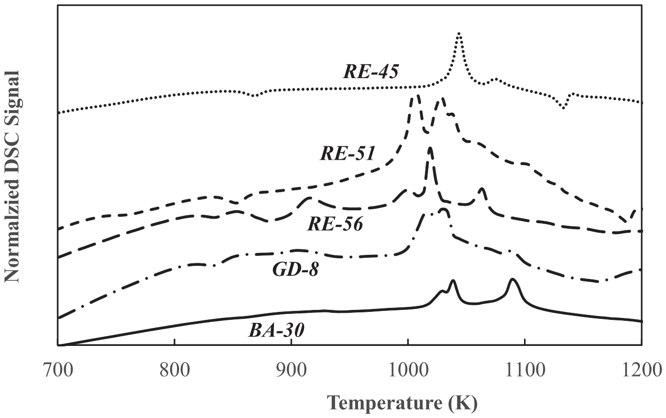

Fig. 1. DSC traces of each batch composition investigated. DSC signal (in μV) was normalized between batches to allow traces to be superimposed. Temperatures are in degrees Kelvin.

3.2. Light output and transparency

The data in Fig. 2 show the light output from a coupon of as-cast glass from each composition relative to that produced from a commercially-available sheet of GOS:Tb. In the as-cast coupons, light output decreased as total rare-earth halide concentration increased (RE-45 through RE-56). Meanwhile, a higher GdF_3 to BaF_2 ratio (BA-30) was found to increase light output in the as cast state.

However, as shown in Fig. 3, this trend did not continue after ceramization. Light output from batch RE-56 far exceeded that from RE-45 and RE-51. Meanwhile, Fig. 4 shows that higher light output was recorded when TbF_3 concentration was increased at the expense of GdF_3 than BaF_2.

Despite improvements in light output with ceramization for batches RE-56 and GD-8 shown above, optical clarity and sample transparency were sacrificed. Fig. 5 shows how sample transparency to 545 nm light (peak emission wavelength) degraded with increased ceramization time for batches GD-8 and RE-56, while transmission at 545 nm in the other compositions was mostly unaffected.

3.3. X-ray diffraction

XRD spectra for cerammed coupons displaying the highest light output from each formulation are shown in Fig. 6. Peak locations were indexed to BaF_2, GdF_3, and TbF_3 reference phases from the ICDD database. Crystalline peaks were obscured by the amorphous

Table 2
Characteristic glass transition (T_g), ceramization (T_{ceram}), and matrix devitrification (T_{dev}) temperatures (in Kelvin) for each glass batch composition, as estimated from DSC traces.

Batch ID	T_g (K)	T_{ceram} (K)	T_{dev} (K)
RE-45	703	858	1043
RE-51	758	843	1003
RE-56	838	863	1008
GD-8	819	859	1014
BA-30	753	848	1028

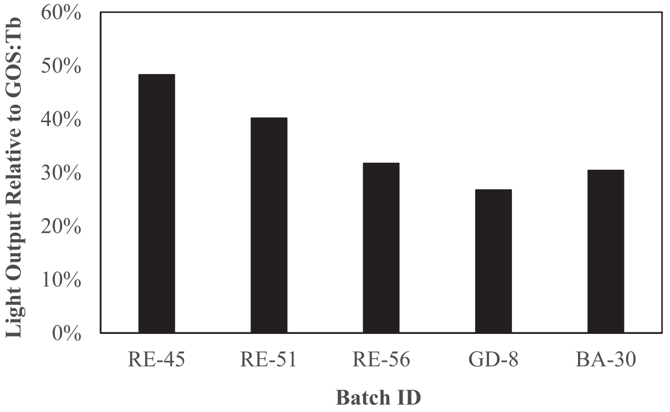

Fig. 2. Light output for as-cast coupons of each batch composition. Values are reported as a percentage of the light output recorded from a commercially-available GOS:Tb coupon.

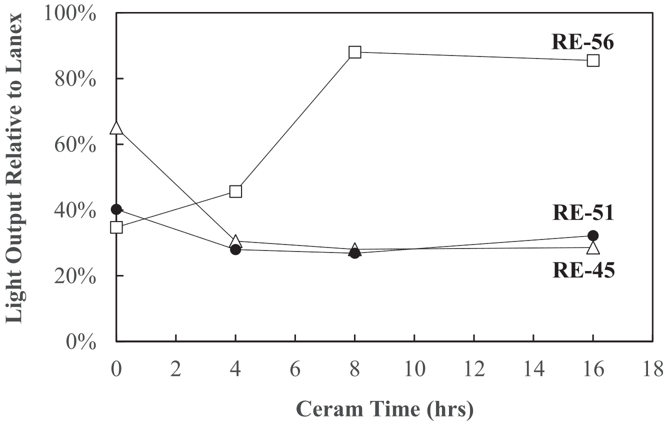

Fig. 3. Light output as a function of ceramization time as rare-earth content was increased from 45 mol% to 56 mol%. Values are reported as a percentage of the light output recorded from a commercially-available GOS:Tb coupon. Lines are a guide for the eye.

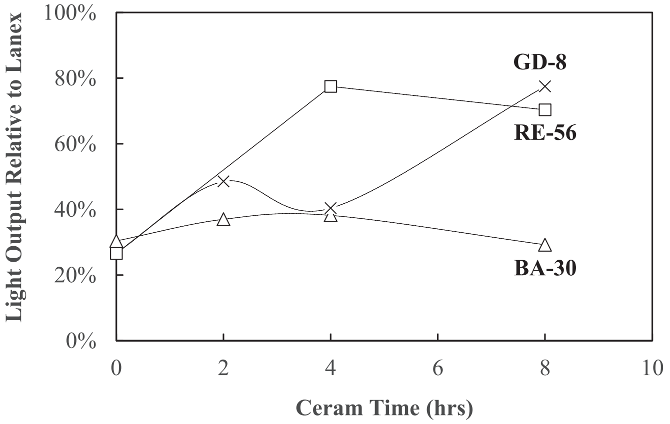

Fig. 4. Light output as a function of ceramization time for batches with increased Tb^{3+} content at the expense of GdF_3(GD-8) and BaF_2 (BA-30) relative to the RE-56 baseline composition. All batches had the same total rare-earth concentration (56 mol%). Values are reported as a percentage of the light output recorded from a commercially-available GOS:Tb coupon. Lines are a guide for the eye.

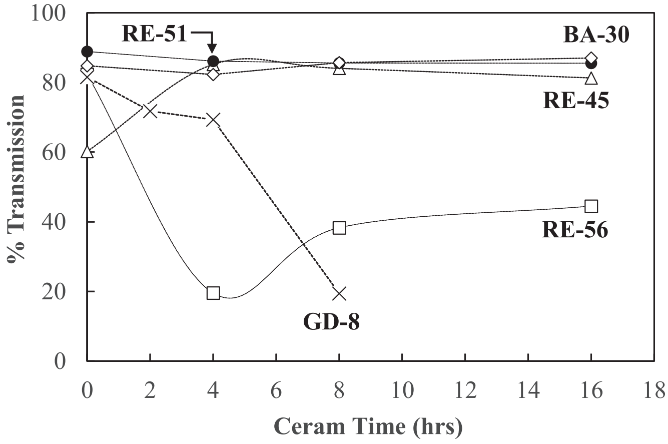

Fig. 5. Changes in transmission at 545 nm for each batch after ceramization step. Lines are a guide for the eye.

halo and background counts for formulations BA-30 and RE-45, and peaks barely emerged over the background for batch RE-51. For spectra that exhibited distinct peaks (RE-56 and GD-8) crystallite sizes were estimated using the Scherrer equation, and calculated as 40 nm and 32 nm, respectively.

TEM images acquired for the coupon of RE-56 cerammed for 8 h at 873K, which produced the highest measured light output, are shown in Fig. 7. An image of the same composition in the as cast state is also included for comparison. The specimen contains spherical crystallites that are approximately 30–40 nm in diameter and have coalesced into snowflake-like clusters that are 200 nm across. These clusters of crystallites are thought to be the reason that the coupons became translucent after ceramization.

3.4. Photoluminescence behavior

The luminescence emission and excitation spectra for batches of increasing rare-earth halide concentration are shown in Fig. 8. The highest intensity peak at 543 nm is attributed to $^5D_4 \rightarrow {}^7F_5$ transitions within the Tb^{3+} energy levels. Secondary emission peaks are also visible at 491 nm, 588 nm, and 623 nm and result from $^5D_4 \rightarrow {}^7F_6$, $^5D_4 \rightarrow {}^7F_4$, and $^5D_4 \rightarrow {}^7F_3$ transitions, respectively, though these peaks are less useful for imaging applications. The location of emission peaks did not shift over the composition range studied, which indicates that the environment surrounding the Tb^{3+} activator remained relatively stable as rare-earth concentration increased. Similarly, the peak positions in the excitation spectra did not show discernible shifts with increasing rare-earth content. The highest intensity excitation peak occurred at 367 nm, which indicates excitation primarily occurred via 4f-5d transitions in the Tb^{3+} energy levels. This correlates with the absorption peaks observed in the transmission spectra shown in Fig. 9. A small peak is visible around 288 nm and corresponds to excitation of Gd^{3+}. However, the much lower intensity relative to Tb^{3+} indicates that excitation primarily occurs in the activator. The location of the excitation peaks also showed minimal changes, suggesting that energy absorption mechanisms remain fairly consistent regardless of rare-earth content. The cause of the much higher intensity 270 nm and 290 nm peaks in the excitation spectrum of RE-45 was unclear, as similar intense absorption as not observed in the transmission spectrum, and so is the subject of current investigations.

The luminescence emission and excitation spectra for batches with increasing TbF_3 at the expense of BaF_2 and GdF_3 are shown in Fig. 10, with transmission data for the same batches shown in Fig. 11. As with the other batches, the peak emission intensity at

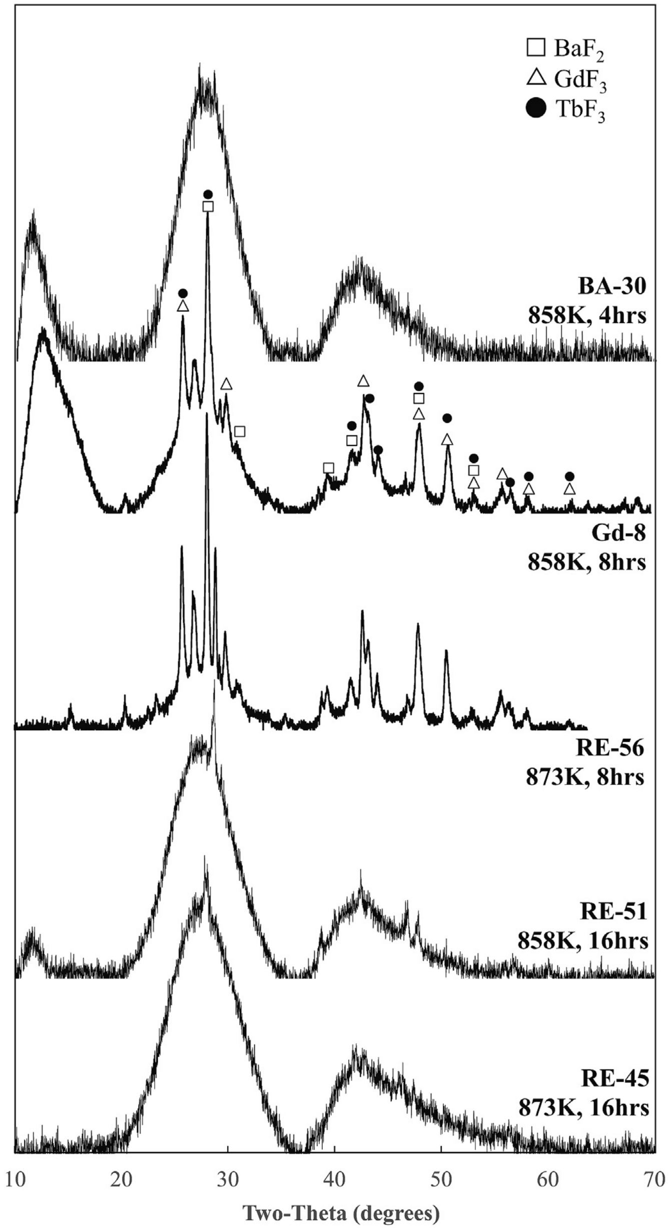

Fig. 6. XRD spectra for cerammed glass-ceramic specimens from each composition that produced the highest light output. Peaks were indexed to GdF_3, BaF_2, and TbF_3 PDF standards.

543 nm due to recombination from $^5D_4 \rightarrow {}^7F_5$ levels in Tb^{3+} dominated, with smaller peaks visible from other recombination modes, mentioned previously. Transmission varied minimally when Gd:Ba ratio was modified, with all coupons exhibiting nearly 80% transmission above 400 nm.

After coupons from all batch compositions were cerammed, the excitation peak locations exhibited negligible shifts with varied ceramization time or composition, as shown in Fig. 12. No changes in emission peak locations (543 nm) were recorded.

4. Discussion

The design of glass formulations and processing protocols for glass-ceramic scintillators is an exercise in compromise, and, given the multi-component nature of the glass system selected, a parametric study was unavoidable. The present investigation sought to manipulate those components and processing parameters that display the most pronounced effect on scintillator light output. The first step was to increase the rare-earth halide content incorporated into the host glass in order to maximize the fraction of material capable of scintillation. The goal was to circumvent the primary disadvantage of composite scintillators relative to single crystals, which is that, by definition, only a fraction of the total volume contributes scintillation photons when excited. However, when rare-earth halide content becomes that majority constituent, similar concentration quenching effects as those observed in single crystals begin to emerge [15]. Recorded light output for as-cast glass decreased at elevated rare-earth concentrations (shown in Fig. 2), despite the fact that all coupons in the RE-45 to RE-56 series were transparent with no visible phase separation or spontaneous crystallization (Fig. 9).

It would have been logical to assume that this degradation in light output at elevated rare-earth concentration would only be exacerbated following ceramization of the as-cast glass coupons. However, Fig. 3 shows that the opposite was actually observed. Light output for cerammed coupons of RE-45 and RE-51 decreased upon ceramization for any duration of time, while the light output for RE-56 actually increased. Minimal changes were observed in the transmission of coupons of RE-45 and RE-51 after ceramization (Fig. 5), and so scattering or absorption due to large crystallites was likely not the source of the reduced light output. This was supported by structural characterization data, as the XRD spectra for these two compositions (shown in Fig. 6) exhibited minimal crystallite formation after ceramization. This was consistent with the lack of an exothermic crystallization peak in the DSC scans of Fig. 1, and suggests that the appropriate temperature needed to induce growth of the rare-earth crystallites was not achieved.

This behavior continued in the RE-56, GD-8, BA-30 series that increased TbF_3 at the expense of GdF_3 and BaF_2, respectively. An exothermic crystallite precipitation peak was not recorded in the DSC trace for BA-30 and no crystallization peaks were observed in the XRD spectrum for a coupon cerammed at 873K for 4 h. Meanwhile, the same GdF_3 and TbF_3 crystalline phases identified after ceramization of RE-56 were recorded for GD-8, with a comparable decrease in transmission observed. The cerammed coupons from GD-8 also acquired a translucent appearance after ceramization, similar to that seen in RE-56. The cause of this reduced transparency may be explained by the clustered nanocrystals seen in the TEM micrographs of cerammed RE-56, shown in Fig. 7. Although the individual crystallites were 30–50 nm (consistent with the broadened XRD peaks and Scherrer calculations), they aggregated into clusters that were much larger. The 200 nm cluster size enters the regime at which visible light begins to scatter, and thus caused the degradation in transparency observed.

These unexpected results prompted a more in depth review of the literature to identify the cause of the deviation from expected trends. Data reported by other authors indicated that a lack of distinguishable exotherms in the DSC trace is a common problem despite the fact that the ability to accurately determine ceramization temperature heavily influences process optimization efforts. For example, Karmakar et al. [16]. had difficulty resolving ceramization peaks from background signal of a $BaGdF_5$-doped oxyfluoride glass even at a heating rate of 30K/min, and Lakshminarayana [17] observed similar inconsistencies in trace features for CeF_3 incorporated into oxyfluoride host glasses. Both investigators only changed the concentration of two glass constituents, but saw considerable variations in thermal analysis measurements. Thus, the present author's difficulties are in good company, even if the convoluted DSC traces render process optimization work more difficult and imprecise.

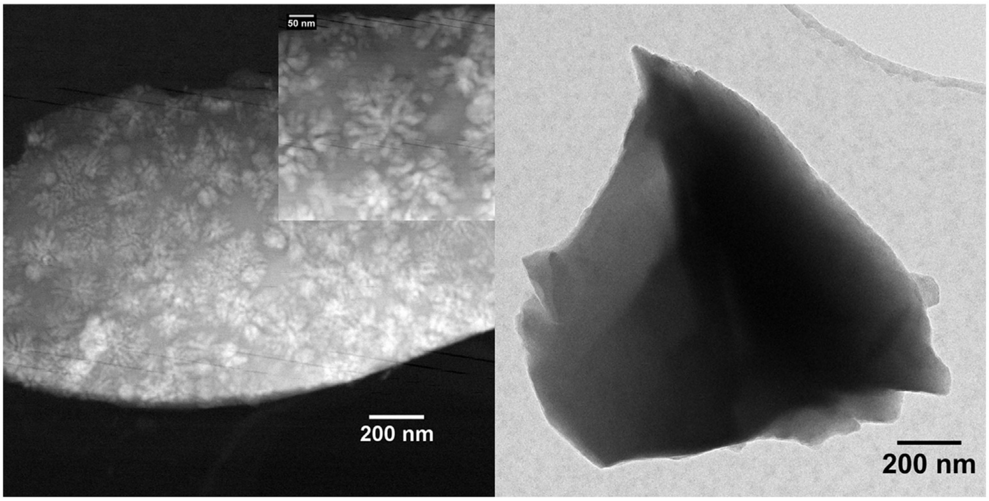

Fig. 7. TEM micrograph of RE-56 cerammed for 8 h at 873K (left) and in the as cast state (right). Small (30 nm) crystallites have coalesced into 200 nm, snowflake-like clusters in the cerammed coupon.

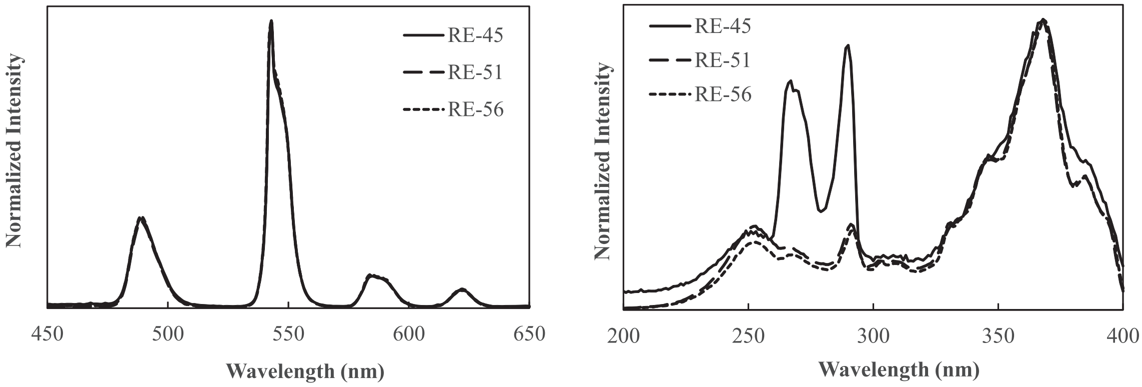

Fig. 8. Photoluminescence emission (left) and excitation (right) spectra for batches with increasing rare-earth halide content. Shifts in peak wavelength with increased rare-earth halide content were negligible as illustrated by the nearly superimposed emission peaks for batches RE-45 through RE-56.

Work by previous authors also provided insight into the cause of decreased light output without a corresponding change in PL-PLE or transmission behavior observed for cerammed coupons from batches RE-45, RE-51, and B-30. Investigation of the crystal nucleation and growth kinetics indicated that nuclei formation is strongly dependent on the time and temperature used in the nucleation step [18]. Nuclei that are below a critical size can actually dissolve back into solution when the glass is reheated to the ceramization (crystal growth) temperature, especially if the heating rate is high [19]. Based on trends observed in previous investigations [10], the current study assumed that nuclei formed during the anneal, which would make a separate nucleation step prior to crystal growth unnecessary, and, thus, a separate nucleation step was not performed. Furthermore, heating rates in excess of 20K/min were used during ceramization, which likely intensified nuclei dissolution [20]. This complete loss of short- or medium-range order in the glass most likely caused the degradation in light output observed in cerammed coupons from batches RE-45, RE-51, and BA-30. This underscores the need for future investigations to identify more reliable means by which to estimate characteristic temperatures used to produce glass-ceramics.

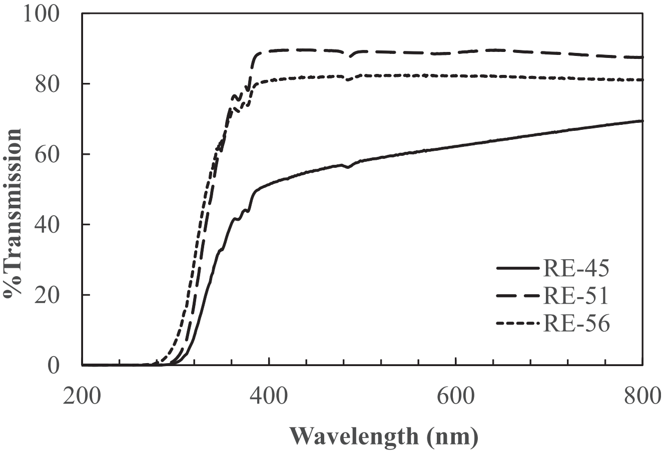

Fig. 9. Transmission spectra for batches of increasing rare-earth halide content. The dips at 377 nm and 488 nm are attributed to absorption due to electron transitions in Tb^{3+}.

5. Conclusions

The effects of composition modifications and ceramization schedules on light output for several rare-earth doped oxyfluoride glasses was investigated. The glass-ceramics are targeted to replace

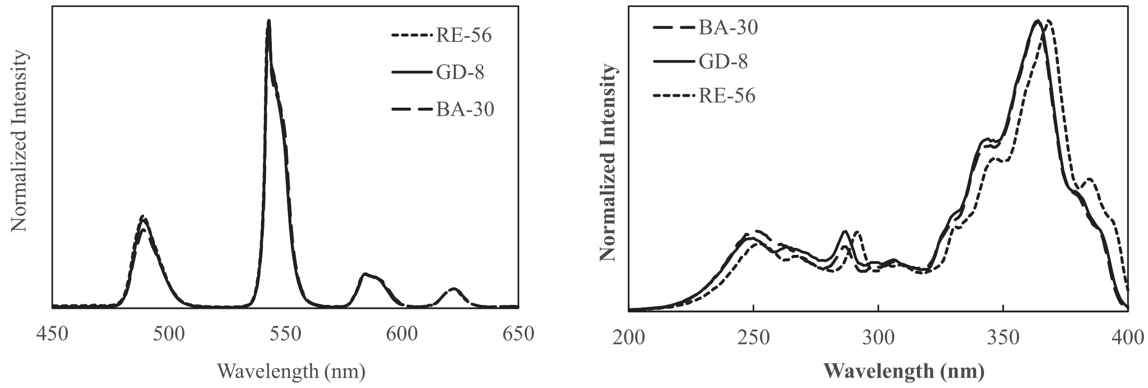

Fig. 10. Luminescence emission (left) and excitation (right) spectra for formulations with increased (GD-8) and decreased (BA-30) ratio of GdF_3 to BaF_2. As with the previous batches, shifts in peak location are negligible, particularly in the emission spectra.

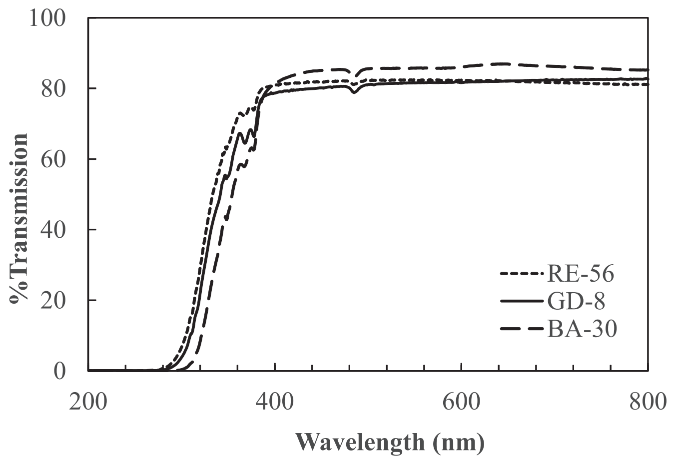

Fig. 11. Transmission data for formulations with increased (GD-8) and decreased (BA-30) ratio of GdF_3 to BaF_2. As with the previous compositions, the dips at 377 nm and 488 nm are attributed to absorption via electron transitions in Tb^{3+}.

or serve as an alternative to current luminescent panels comprised of GOS:Tb phosphor-loaded polymers or CsI:Tl single crystals. The glass-ceramics displayed good progress in meeting the performance metrics set by these industry standards, though the key metric (light output) is still below the target values. Based on data collected in this investigation, next steps should focus on more precise determination of crystallite nucleation and growth temperatures specific to each composition in order to ensure scintillating crystallites reach the targeted size (30–50 nm) and do not dissolve back into the glass matrix. This will facilitate more efficient capture and conversion of incident X-ray energy into visible photons that can be used in image creation for diagnostic and therapeutic medical imaging.

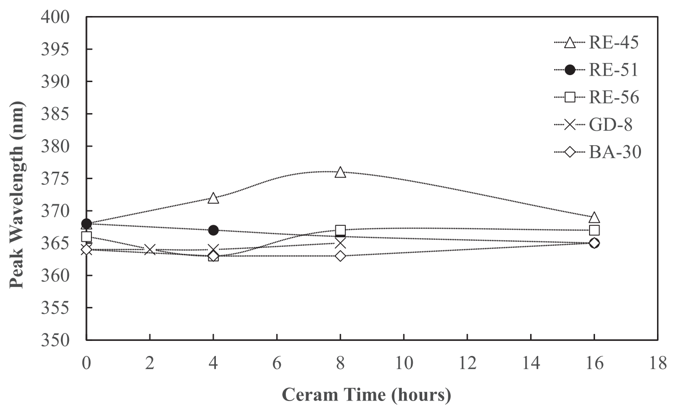

Fig. 12. Changes in excitation peak wavelength after ceramization of each composition. No changes were observed in emission peak location. Lines are a guide for the eye.

Acknowledgements

This work was made possible by generous support from the Coulter Foundation Translational Research Partnership.

References

[1] C.W.E. Van Eijk, Inorganic scintillators in medical imaging, Phys. Med. Biol. 47 (2002) R85–R106.
[2] J. E. Mathers and R. L. Yale, Terbium-activated gadolinium oxysulfide X-ray phosphor, 4,507,560, 1985.
[3] O. Svenonius, A. Sahlholm, P. Wiklund, J. Linnros, Performance of an X-ray imaging detector based on a structured scintillator, Nucl. Instrum. Methods Phys. Res. Sect. A Accel. Spectrom. Detect. Assoc. Equip. 607 (1) (Aug. 2009) 138–140.
[4] E. Samei, Performance of digital radiographic detectors: quantification and assessment methods, Adv. Digit. Radiogr. RSNA Categ. course Diagn. Radiol. Phys. 2003 27710 (2003) 37–47.
[5] N.J. Cherepy, J.D. Kuntz, Z. Seely, S. Fisher, O.B. Drury, B. Sturm, Transparent ceramic scintillators for gamma-ray spectroscopy and radiography, SPIE (2010). Article 780501.
[6] N.J. Cherepy, S.A. Payne, B.W. Sturm, S.P. O'Neal, Z.M. Seeley, O.B. Drury, L.K. Haselhorst, B.L. Rupert, R.D. Sanner, P.A. Thelin, S.E. Fisher, R. Hawrami, K.S. Shah, A. Burger, J.O. Ramey, L.A. Boatner, Performance of Europium-doped strontium iodide, transparent ceramics and bismuth-loaded polymer scintillators, Proc. SPIE 8142 (2011), 81420W–81420W-8.
[7] W. Cai, Q. Chen, N.J. Cherepy, A. Dooraghi, D. Kishpaugh, A. Chatziioannou, S. Payne, W. Xiang, Q. Pei, Synthesis of bulk-size transparent gadolinium oxide–polymer nanocomposites for gamma ray spectroscopy, J. Mater. Chem. C 1 (2013) 1970.
[8] M. Nikl, Scintillation detectors for x-rays, Meas. Sci. Technol. 17 (4) (2006) R37–R54.
[9] M.B. Barta, J.H. Nadler, Z. Kang, B.K. Wagner, R. Rosson, Y. Cai, K.H. Sandhage, B. Kahn, Composition optimization of scintillating rare-earth nanocrystals in oxide glass-ceramics for radiation spectroscopy, Appl. Opt. 53 (16) (Jun. 2014) D21–D28.
[10] M.B. Barta, J.H. Nadler, Z. Kang, B.K. Wagner, R. Rosson, B. Kahn, Effect of host glass matrix on structural and optical behavior of glass–ceramic nanocomposite scintillators, Opt. Mater. (Amst). 36 (2) (Dec. 2013) 287–293.
[11] A.V. Gektin, A. Belsky, A.N. Vasil, Scintillation efficiency improvement by mixed crystal use, IEEE Trans. Magn. 61 (1) (2014) 262–270.
[12] A.V. Gektin, B. Grinyov, A. Belsky, Phenomenological approach to prediction of scintillation yield in mixed crystals, in: International Conference on Oxide Materials for Electronic Engineering, 2014, pp. 243–244.
[13] Z. Shan, D. Chen, Y. Yu, P. Huang, H. Lin, Y. Wang, Luminescence in rare earth-doped transparent glass ceramics containing GdF3 nanocrystals for lighting applications, J. Mater. Sci. 45 (10) (2010) 2775–2779.
[14] C. Zhang, J. Wang, C. Song, Y. Shang, S. Shen, BaGdF5:Ce3+, Ln3+ (Ln=Eu and Tb) nanoparticles: tunable multicolor emission and magnetic property, Mater. Lett. 118 (2014) 88–91.

[15] B.M. Tissue, Synthesis and luminescence of lanthanide ions in nanoscale insulating hosts, Chem. Mater. 10 (10) (Oct. 1998) 2837–2845.
[16] P. Karmakar, A.K. Subudhi, K. Biswas, K. Annapurna, Crystallization kinetics analysis of BaF2 and BaGdF5 nanocrystals precipitated from oxyfluoride glass systems: a comparative study, Thermochim. Acta 610 (Jun. 2015) 1–9.
[17] G. Lakshminarayana, E.M. Weis, B.L. Bennett, A. Labouriau, D.J. Williams, J.G. Duque, M. Sheik-Bahae, M.P. Hehlen, Structural, thermal, and luminescence properties of cerium-fluoride-rich oxyfluoride glasses, Opt. Mater. (Amst). 35 (2) (Dec. 2012) 117–125.
[18] C. Bocker, C. Russel, Self-organized nano-crystallization of BaF2 from Na2O/K2O/BaF2/Al2O3/SiO2 glasses, J. Eur. Ceram. Soc. 29 (2009) 1221–1225.
[19] M.J. Davis, Effect of the growth treatment on two-stage nucleation experiments, J. Am. Ceram. Soc. 84 (3) (2001) 492–496.
[20] C. Rüssel, R. Keding, A new explanation for the induction period observed during nucleation of lithium disilicate glass, J. Non Cryst. Solids 328 (1–3) (2003) 174–182.